Mon. Not. R. Astron. Soc. **391,** 320–333 (2008) doi:10.1111/j.1365-2966.2008.13885.x

Exploring the substellar temperature regime down to ∼550 K

Ben Burningham,[1⋆] D. J. Pinfield,[1] S. K. Leggett,[2] M. Tamura,[3] P. W. Lucas,[1] D. Homeier,[4] A. Day-Jones,[1] H. R. A. Jones,[1] J. R. A. Clarke,[1] M. Ishii,[5] M. Kuzuhara,[6] N. Lodieu,[7] M. R. Zapatero Osorio,[7] B. P. Venemans,[8] D. J. Mortlock,[9] D. Barrado y Navascués,[10] E. L. Martin[7] and A. Magazzù[11]

[1]*Centre for Astrophysics Research, Science and Technology Research Institute, University of Hertfordshire, Hatfield AL10 9AB*
[2]*Gemini Observatory, 670 N. A'ohoku Place, Hilo, HI 96720, USA*
[3]*National Astronomical Observatory, Mitaka, Tokyo 181-8588, Japan*
[4]*Institut fur Astrophysik, Georg-August-Universitat, Friedrich-Hund-Platz 1, 37077 Gottingen, Germany*
[5]*Subaru Telescope, 650 North A'ohoku Place, Hilo, Hi 96720, USA*
[6]*University of Tokyo, Hongo, Tokyo 113-0033, Japan*
[7]*Instituto de Astrofísica de Canarias, 38200 La Laguna, Spain*
[8]*Institute of Astronomy, Madingley Road, Cambridge CB3 0HA*
[9]*Astrophysics Group, Imperial College London, Blackett Laboratory, Prince Consort Road, London SW7 2AZ*
[10]*Laboratorio de Astrofísica Espacial y Física Fundamental, INTA, PO Box 78, E-28691 Villanueva de la Canada (Madrid), Spain*
[11]*Fundación Galileo Galilei – INAF, Apartado 565, E-38700 Santa Cruz de La Palma, Spain*

Accepted 2008 August 27. Received 2008 August 13; in original form 2008 June 9

ABSTRACT

We report the discovery of three very late T dwarfs in the UKIRT Infrared Deep Sky Survey (UKIDSS) Third Data Release: ULAS J101721.40+011817.9 (ULAS1017), ULAS J123828.51+095351.3 (ULAS1238) and ULAS J133553.45+113005.2 (ULAS1335). We detail optical and near-infrared (NIR) photometry for all three sources, and mid-IR photometry for ULAS1335. We use NIR spectra of each source to assign spectral types T8p (ULAS1017), T8.5 (ULAS1238) and T9 (ULAS1335) to these objects. ULAS1017 is classed as a peculiar T8 (T8p) due to appearing as a T8 dwarf in the J band, whilst exhibiting H- and K-band flux ratios consistent with a T6 classification. Through comparison to BT-Settl model spectra we estimate that ULAS1017 has $750\,\mathrm{K} \lesssim T_{\rm eff} \lesssim 850\,\mathrm{K}$, and $5.0 \lesssim \log g(\mathrm{cm\,s^{-2}}) \lesssim 5.5$, assuming solar metallicity. This estimate for gravity is degenerate with varying metallicity. We estimate that ULAS1017 has an age of 1.6–15 Gyr, a mass of 33–70M_J and lies at a distance of 31–54 pc. We do not estimate atmospheric parameters for ULAS1238 due to a lack of K-band photometry. We extend the unified scheme of Burgasser et al. to the type T9 and suggest the inclusion of the W_J index to replace the now saturated J-band indices. We propose ULAS1335 as the T9 spectral type standard. ULAS1335 is the same spectral type as ULAS J003402.77−005206.7 and CFBDS J005910.90−011401.3. We argue that given the similarity of the currently known >T8 dwarfs to the rest of the T dwarf sequence, the suggestion of the Y0 spectral class for these objects is premature. Comparison of model spectra with that of ULAS1335 suggest a temperature below 600 K, possibly combined with low gravity and/or high metallicity. We find ULAS1335 to be extremely red in NIR to mid-IR colours, with $H - [4.49] = 4.34 \pm 0.04$. This is the reddest NIR to mid-IR colour yet observed for a T dwarf. The NIR to mid-IR spectral energy distribution of ULAS1335 further supports $T_{\rm eff} < 600$ K, and we estimate $T_{\rm eff} \sim 550$–600 K for ULAS1335. We estimate that ULAS1335 has an age of 0.6–5.3 Gyr, a mass of 15–31M_J and lies at a distance of 8–12 pc.

Key words: surveys – stars: low-mass, brown dwarfs.

1 INTRODUCTION

Extending the known sample of field dwarfs to ever lower effective temperatures ($T_{\rm eff}$) is important not only for the determination of the

⋆E-mail: b.burningham@herts.ac.uk

field mass function, but also for probing temperature and pressure regimes that have hitherto been unexplored observationally. The study of extremely cool brown dwarfs opens a window on atmospheric physics which will be fundamental for understanding the processes within a broad range of substellar atmospheres, including those of giant exoplanets.

At the time of writing there are 142 T dwarfs published in the literature (e.g. DwarfArchives.org; Pinfield et al. 2008). Of these, only five are classified as T8 or later (using the scheme of Burgasser et al. 2006), two of which have spectral types later than T8: ULAS J003402.77−005206.7 (hereafter ULAS0034; Warren et al. 2007) and CFBDS J005910.90−011401.3 (hereafter CFBDS0059; Delorme et al. 2008). ULAS0034 has an inferred $T_{\rm eff}$ of 600–700 K (Warren et al. 2007), and Delorme et al. (2008) infer a $T_{\rm eff}$ for CFBDS0059 that is ∼50 K cooler than that of ULAS0034.

Expanding the sample of very cool brown dwarfs, and exploring possible factors that could motivate the implementation of new spectral classes (e.g. Y dwarfs; Kirkpatrick et al. 1999) are primary science drivers for the UKIRT Infrared Deep Sky Survey (UKIDSS) Large Area Survey (LAS; see Lawrence et al. 2007). Our collaboration, the UKIDSS Cool Dwarf Science Working Group (CDSWG) is engaged in a substantial effort to achieve this aim (e.g. Kendall et al. 2007; Lodieu et al. 2007; Warren et al. 2007; Pinfield et al. 2008). Here we present the recent discovery by CDSWG of three very cool brown dwarfs. These are ULAS J101721.40+011817.9 (ULAS1017), ULAS J123828.51+095351.3 (ULAS1238) and ULAS J133553.45+113005.2 (ULAS1335). The last of these, ULAS1335, may be the coolest brown dwarf yet discovered and we here discuss the properties of this object, estimating a $T_{\rm eff}$ of approximately 550–600 K.

2 SOURCE IDENTIFICATION

The objects presented here were selected from the third data release (DR3) of UKIDSS (Warren et al., in preparation). We used the same method as that outlined in sections 2 and 3 of Pinfield et al. (2008). The process of identifying and confirming extremely late T dwarfs can be separated into three principle stages: (1) initial selection by mining survey data; (2) confirmation of photometric properties by near-infrared (NIR) and optical follow-up; (3) NIR spectroscopy to estimate spectral type. The Gemini/NIRI spectroscopic follow-up took place in two stages in queue mode. Initial, short ($t_{\rm int}$ = 16 min) *J*-band observations were obtained first. These initial spectra confirmed that two of our targets were indeed of extremely late spectral type, and deeper *J*-, *H*- and *K*-band observations were then queued. Subaru/IRCS spectroscopic follow-up took place separately for additional candidates in classical mode and confirmed the very late-type of a third target. We will discuss each of these stages in more detail in the following sections.

2.1 Mining UKIDSS DR3

We initially searched the UKIDSS LAS data for sources that met colour criteria: $Y-J > 0.5$; $J-H < 0.1$; $\sigma < 0.3$, where σ is the uncertainty in the magnitude measured in each of the three *YJH* bands. The resultant candidate list was cross-matched against the Sloan Digital Sky Survey (SDSS) Data Release 6 (DR6) using a pairing radius of 2 arcsec. Objects with no SDSS counterpart, or whose SDSS–UKIDSS $z' - J > 3.0$, were retained as potential candidates. We identified some 50 candidate T dwarfs in this search. ULASJ1238 and ULASJ1335 were picked out for immediate and rapid follow-up due to survey colours that were reminiscent of the prototype >T8 dwarf ULAS J0034. ULAS1017 on the other hand was selected due to its extremely blue $J - H$ colour from UKIDSS photometry.

2.2 Ground-based photometric follow-up

NIR follow-up photometry was obtained using the UKIRT Fast Track Imager (UFTI; Roche et al. 2003) mounted on UKIRT, and the Long-slit Infrared Imaging Spectrograph (LIRIS; Manchado et al. 1998) mounted on the William Herschel Telescope on La Palma. The mosaics were produced using sets of jittered images, with individual exposure times, jitter patterns and number of repeats given in Table 1. The data were dark subtracted, flat-field corrected, sky subtracted and mosaicked using ORAC-DR for the UFTI data, and LIRIS-DR for the LIRIS data. We calibrated our UFTI observations using UKIRT Faint Standards (Leggett et al. 2006), with a standard observed at a similar airmass for each target. All UFTI data were obtained under photometric conditions, with seeing better than 0.9 arcsec. The wider field LIRIS data were obtained through thin cirrus in variable seeing (0.8–2.0 arcsec) and were calibrated against Two Micron All Sky Survey (2MASS) stars within the field of view. LIRIS uses a $K_{\rm s}$ filter, and as such no transform was required for the 2MASS stars. The $K_{\rm s}$ magnitude for ULAS1017 was transformed to the MKO system using the transform derived by Pinfield et al. (2008).

We have also obtained optical *z*-band photometry using the ESO Multi-Mode Instrument (EMMI) mounted on the New Technology Telescope at La Silla, Chile on the nights of 2008 January 29 and

Table 1. Summary of the observations obtained for NIR and optical photometric follow-up. The breakdown of each integration is given in the final column with the following notation: j = number of jitter points; r = number of repeats for jitter pattern; $t_{\rm exp}$ = exposure time at each jitter point.

Object	Filter	Instrument	UT date	Total integration time (s)	$t_{\rm int}$ breakdown
ULAS1017	*J*	UFTI	2008 January 17	300	($j = 5, r = 1, t_{\rm exp} = 60$ s)
	H	UFTI	2008 January 17	2400	($j = 5, r = 6, t_{\rm exp} = 60$ s)
	K_s	LIRIS	2008 March 17	2400	($j = 5, r = 24, t_{\rm exp} = 20$ s)
	$z_{\rm EMMI}$	EMMI	2008 January 30	2400	($j = 1, r = 4, t_{\rm exp} = 600$ s)
ULAS1238	*J*	UFTI	2008 January 25	300	($j = 5, r = 1, t_{\rm exp} = 60$ s)
	H	UFTI	2008 January 25	1800	($j = 5, r = 6, t_{\rm exp} = 60$ s)
	$z_{\rm EMMI}$	EMMI	2008 January 30	2400	($j = 1, r = 4, t_{\rm exp} = 600$ s)
ULAS1335	*Y*	UFTI	2008 January 16	540	($j = 9, r = 1, t_{\rm exp} = 60$ s)
	J	UFTI	2008 January 16	300	($j = 5, r = 1, t_{\rm exp} = 60$ s)
	H	UFTI	2008 January 16	900	($j = 5, r = 3, t_{\rm exp} = 60$ s)
	K	UFTI	2008 January 16	900	($j = 5, r = 3, t_{\rm exp} = 60$ s)
	$z_{\rm EMMI}$	EMMI	2008 January 29	1200	($j = 1, r = 2, t_{\rm exp} = 600$ s)

Table 2. The available photometry for each of the new ultracool dwarfs. In each case the first row gives survey photometry from UKIDSS LAS (apermag3; see Dye et al. 2006). All three objects were undetected in SDSS DR6. The second row for each object gives the results of the follow-up photometry described in Section 2.2.

Object	Y	J	H	K	z'(AB)	z'(AB) $-$ J	$Y-J$	$J-H$	$H-K$
ULAS1017	19.72 ± 0.15	18.57 ± 0.07	19.38 ± 0.24				1.15 ± 0.17	-0.82 ± 0.25	
		18.53 ± 0.02	19.07 ± 0.02	19.01 ± 0.10	22.49 ± 0.09	3.96 ± 0.09	1.19 ± 0.15	-0.54 ± 0.03	0.06 ± 0.10
ULAS1238	19.55 ± 0.07	18.78 ± 0.06	19.25 ± 0.15				0.77 ± 0.09	-0.47 ± 0.17	
		18.95 ± 0.02	19.20 ± 0.02		22.74 ± 0.12	3.79 ± 0.12	0.60 ± 0.07	-0.25 ± 0.03	
ULAS1335	18.70 ± 0.05	17.90 ± 0.03	18.15 ± 0.12	18.47 ± 0.20			0.80 ± 0.06	-0.25 ± 0.13	-0.32 ± 0.23
	18.81 ± 0.04	17.90 ± 0.01	18.25 ± 0.01	18.28 ± 0.03	22.04 ± 0.10	4.14 ± 0.10	0.91 ± 0.04	-0.35 ± 0.01	-0.03 ± 0.03

30. These observations are summarized in Table 1. For this optical follow-up we used a Bessel z-band filter (ESO Z#611). The data were reduced using standard IRAF packages, and then multiple images of the same target were aligned and stacked to increase signal-to-noise ratio.

We calibrated our z-band photometry using SDSS DR6 sources present in our images as secondary standards. We transformed the Sloan z' (AB) magnitudes to the EMMI system using the transformation given by Warren et al. (2007) before using them to determine zero-points, which had a typical scatter of ± 0.04 mag. The resulting EMMI photometry for our targets was then transformed to the Sloan z'(AB) system (see Warren et al. 2007). The results of our ground-based follow-up photometry are given in Table 2, which also gives the original data base photometry.

2.3 Spectroscopic confirmation

Spectroscopy in the *JHK* bands was obtained for ULAS1238 and ULAS1335 using the Near-Infrared Imager and Spectrometer (NIRI; Hodapp et al. 2003) on the Gemini-North Telescope on Mauna Kea under programmes GN-2007B-Q-26 and GN-2008A-Q-15. The Infrared Camera and Spectrograph (IRCS; Kobayashi et al. 2000) on the Subaru telescope on Mauna Kea was used to obtain the *JH* spectrum for ULAS1017 and this was then followed with spectroscopy in the *H* and *K* bands with Gemini/NIRI. Additionally, we obtained a *Y*-band spectrum for ULAS1335 using the Infrared Spectrometer and Array Camera (ISAAC; Moorwood et al. 1998) mounted on VLT UT1 and ESO, Paranal in Director's Discretionary Time [programme ID: 280.C-5067(A)].

All observations were made up of a set of subexposures in an ABBA jitter pattern to facilitate effective background subtraction, with a slit width of 1 arcsec. The length of the AB jitter was 10 arcsec. The observations are summarized in Table 3. The NIRI observations were reduced using standard IRAF Gemini packages. The Subaru IRCS *JH* spectrum was also extracted using standard IRAF packages. The AB pairs were subtracted using generic IRAF tools, and median stacked. In the case of IRCS, the data were found to be sufficiently uniform in the spatial axis for flat-fielding to be neglected. The ISAAC data were reduced and extracted using the same steps, but implemented with the ESO ISAAC pipeline version 5.7.0.

For all three sets of data, a comparison argon arc frame was used to obtain a dispersion solution, which was then applied to the pixel coordinates in the dispersion direction on the images. The resulting wavelength-calibrated subtracted pairs had a low level of residual sky emission removed by fitting and subtracting this emission with a set of polynomial functions fit to each pixel row perpendicular to the dispersion direction, and considering pixel data on either side of the target spectrum only. The spectra were then extracted using a linear aperture, and cosmic rays and bad pixels removed using a sigma-clipping algorithm.

Telluric correction was achieved by dividing each extracted target spectrum by that of an early A or F type star observed just before or after the target and at a similar airmass. Prior to division, hydrogen lines were removed from the standard star spectrum by interpolating the stellar continuum. Relative flux calibration was then achieved by multiplying through by a blackbody spectrum of the appropriate $T_{\rm eff}$. Data obtained for the same spectral regions on different nights were co-added after relative flux calibration, each weighted by their exposure time.

The spectra were then joined together using the measured NIR photometry to place the spectra on an absolute flux scale, and

Table 3. Summary of the NIR spectroscopic observations.

Object	UT date	Integration time (s)	Instrument	Spectral region
ULAS1017	2008 January 25	12×300	IRCS	*JH*
	2008 March 14	16×225	NIRI	*K*
	2008 May 11	12×300	NIRI	*H*
ULAS1238	2007 December 21	4×240	NIRI	*J*
	2008 January 23	12×300	NIRI	*J*
	2008 January 23	12×300	NIRI	*H*
	2008 February 18	8×225	NIRI	*K*
	2008 February 26	6×225	NIRI	*K*
ULAS1335	2007 December 21	4×240	NIRI	*J*
	2008 January 22	12×300	NIRI	*J*
	2008 January 22	12×300	NIRI	*H*
	2008 February 28	20×225	NIRI	*K*
	2008 March 19	12×300	ISAAC	*Y*

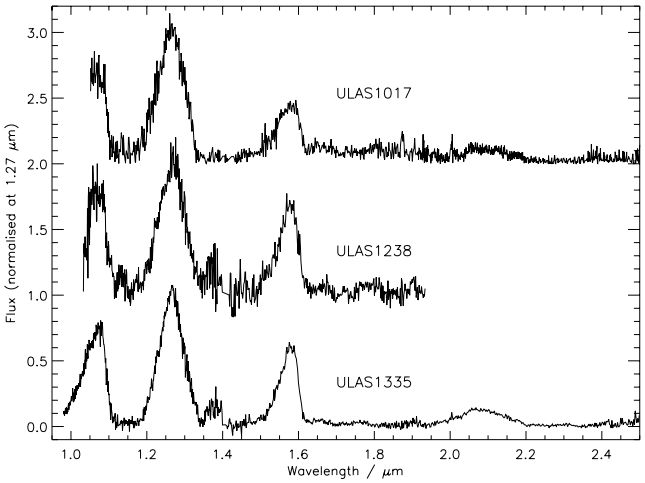

Figure 1. The NIRI *JHK* spectrum for ULAS1335 (bottom), the *JH* spectrum for ULAS1238 (middle). The IRCS *J* and NIRI *HK* spectrum of ULAS1017 is shown on the top row.

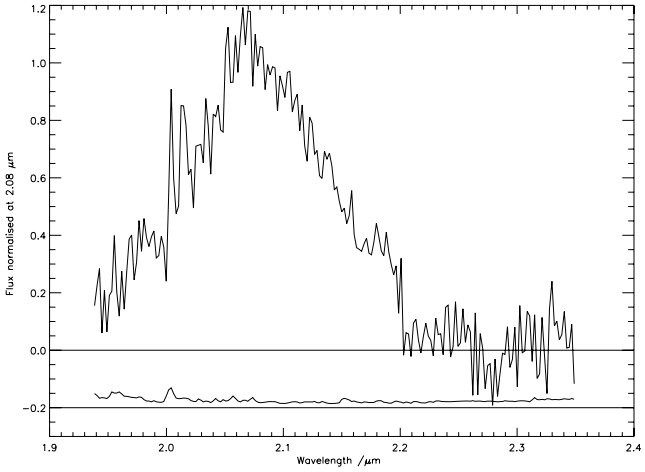

Figure 2. The NIRI *K*-band spectrum for ULAS1238. The error spectrum is shown offset by −0.2.

rebinned by a factor of 3 to increase the signal-to-noise ratio, whilst avoiding undersampling for the spectral resolution. The IRCS *JH* spectrum of ULAS1017 was joined to the NIRI *H*- and *K*-band spectra in a similar way, but the NIRI spectra were rebinned by a factor of 3 prior to joining. The resultant *YJHK* and *JHK* spectra for ULAS1017 and ULAS1335 are shown in Fig. 1, where the combined spectra have been normalized to unity at 1.27 μm and each offset for clarity. In the case of ULAS1238, we have so far been unable to obtain a *K*-band magnitude, so only the *JH* spectrum is shown in Fig. 1, the *K*-band spectrum is shown separately in Fig. 2, normalized to unity at 2.08 μm.

2.4 *Spitzer*–IRAC follow-up of ULAS1335

We obtained IRAC four-channel (3.55, 4.49, 5.73 and 7.87 μm) photometry of the source on 2008 March 5. The data were obtained as part of the *Spitzer Space Telescope* Cycle 4 programme #40449. All four channels have 256 × 256-pixel detectors with a pixel size of 1.2 × 1.2 arcsec^2, yielding a 5.2 × 5.2-arcmin^2 field of view. Two adjacent fields were imaged in pairs (channels 1 and 3; channels 2 and 4) using dichroic beam splitters. The telescope was then nodded to image a target in all four channels.[1] We used exposure times of 30 s and a nine-position medium-sized (52 pixels) dither pattern, for an exposure of 270 s for each channel, and a total observing time of 15.8 min to acquire all channels, slew and settle.

Table 4. Mid-IR photometry for ULAS1335. Random uncertainties are quoted. An additional 3 per cent uncertainty should be added in quadrature to the quoted random uncertainties to account for systematics.

Band (μm)	Magnitude (Vega)
3.55	15.96 ± 0.02
4.49	13.91 ± 0.01
5.73	14.34 ± 0.04
7.87	13.37 ± 0.07

The data were reduced using the post-basic-calibration data mosaics generated by version 17.0.4 of the IRAC pipeline.[2] The mosaics were flat-fielded and flux-calibrated using superflats and global primary and secondary standards observed by *Spitzer*. We performed aperture photometry using an aperture with a 2 pixel (or 2.4 arcsec) radius, to maximize the signal-to-noise ratio. The object was relatively isolated with the closest source ∼7 arcsec away. The object appears single in the IRAC images, as in the case of the NIR images. To convert to total fluxes, we applied aperture corrections as described in chapter 5 of the IRAC Data Handbook of 1.205, 1.221, 1.363 and 1.571 to channels 1–4, respectively. The photometry was converted from mJy to magnitudes on the Vega system using the zero-magnitude fluxes given in the IRAC Data Handbook (280.9, 179.7, 115.0 and 64.1 Jy for channels 1–4, respectively). Photometric errors were derived from the uncertainty images that are provided with the post-basic-calibration data. The magnitudes and errors are given in Table 4. Note that in addition to the errors in the table, there are absolute calibration uncertainties of 2–3 per cent. There are also systematic uncertainties introduced by pipeline dependencies of comparable magnitude (Leggett et al. 2007b). We adopt the total photometric uncertainty to be the sum in quadrature of the values given in Table 4 plus 3 per cent.

3 SPECTRAL TYPES

Two methods for establishing spectral type are used. The first is by comparison of our spectra to the spectra of T spectral type standards as defined by Burgasser et al. (2006). Since the latest spectral type defined by that system is T8, for which the standard is 2MASS J04151954−0935066 (hereafter 2MASS0415), we also compare our spectra to the two previously identified T8+ objects, ULAS0034 and CFBDS0059.

The *Y*- and *K*-band morphologies are more strongly dependent on metallicity and gravity than the *J* and *H* bands. This is due to the influence of pressure-dependent collisionally induced H_2 absorption in the *K* band (e.g. Burgasser et al. 2002), and the red side of the *Y*-band flux peak (Allard et al., in preparation). In addition,

[1] For more information about IRAC, see Fazio et al. (2004) and the IRAC Users Manual at http://ssc.spitzer.caltech.edu/irac/descrip.html.
[2] Information about the IRAC pipeline and data products can be found at http://ssc.spitzer.caltech.edu/irac/dh/.

the blue side of the *Y*-band peak is shaped by the red wing of the broad K I absorption centred at 7700 Å, which is strongly dependent on metallicity (Burrows et al. 2002). As such we base our spectral types on the comparisons of the *J*- and *H*-band spectra of our objects. In this case we normalize our *J*- and *H*-band spectra to unity at 1.27 and 1.58 μm, respectively, to facilitate comparison of their relative shapes, rather than heights (which will be discussed separately).

The second method for establishing type is the use of the T dwarf spectral indices, calculated as flux ratios, which are also defined by Burgasser et al. (2006). Aware that some spectral indices may become saturated for types later than T8, we place our emphasis for determining type on the template comparison, and use this to assess the validity of the defined spectral indices.

Delorme et al. (2008) argue that ULAS0034 and CFBDS0059 may represent the transition to Y spectral class due to the onset of broad NH_3 absorption in the blue side of the *H*-band flux peak. They put forward the NH_3–*H* ratio as a spectral index, and suggest that it traces the strength of ammonia absorption (see Table 5). However, given the absence of calculated ammonia opacities in the NIR, and possible influence of nearby water absorption band we do not feel that this identification is certain. Pending further confirmation of this feature, we will refer to this index as 'NH_3'–*H*. Whether the absorption feature attributed to ammonia by Delorme et al. (2008) is indeed the first defining feature of the Y class will depend on how this feature develops towards lower temperatures and as more objects in this regime are identified.

We calculate the W_J and 'NH_3'–*H* spectral indices as put forward by Warren et al. (2007) and Delorme et al. (2008), respectively. The W_J index traces the decreasing width of the *J*-band peak through the ratio of flux in a section of the blue slope of the peak to that in the crown. As such the value W_J index is driven by the strength of the *J*-band water absorption. These indices and the flux ratios from which they are derived are given in Table 5 for the three objects we have introduced, in addition to those for the T8 standard 2MASS0415 and the two previously discovered T8+ objects. The final two columns of Table 5 give the implied type from the template comparison and the spectral type we adopt for each object, as discussed in more detail in the following sections.

3.1 ULAS1017

The spectrum of ULAS1017 has a peculiar property. It appears to have a different spectral type in the *H*- and *K*-band flux peaks as compared to the *J*-band peak. Fig. 3 shows the comparison of our IRCS + NIRI spectrum for ULAS1017 with the T8 standard 2MASS0415 and the T6 standard SDSS J162414.37+002915.6 (hereafter SDSS1624). ULAS1017 traces the form of the T8 spectrum well in the *J* band, but the *H*-band peak matches the T6 spectrum best, particularly towards the red end of this region. This is reflected in the calculated spectral indices for this object (see Table 5). We adopt therefore the type T8p for this object.

We do not think such morphology could arise as a result of a T8 + T6, or similar, unresolved binary, as flux from the brighter T6 would tend to fill in the deep absorption feature in the *J* band, where we see very little flux in this case. Furthermore, spectral synthesis using various binary components, following the method of Burgasser et al. (2008), is not able to reproduce the spectral ratios seen for this object. The problem arises because earlier type objects, which can reproduce the *H* and *K* bands tend to dominate the light, and drive the ratios in the *J* band to earlier values also. Although *J*-band flux reversals have been observed elsewhere (e.g. Looper

Table 5. The NIR spectral index ratios as defined by Burgasser et al. (2006) for the three objects presented in this paper, and for the T8 standard 2MASS0415 and the previously discovered T8+ dwarfs. Also given is the W_J index as defined by Warren et al. (2007), and the 'NH_3'–*H* index defined by Delorme et al. (2008). The final two columns give the spectral type from template comparison in the Burgasser et al. (2006) scheme, and the final adopted spectral type.

Index	H_2O-J	CH_4-J	W_J	H_2O-H	CH_4-H	'NH_3'–*H*	CH_4-K	*K*/*J*	Template	Type
Flux ratio	$\frac{\int_{1.14}^{1.165} f(\lambda)d\lambda}{\int_{1.26}^{1.285} f(\lambda)d\lambda}$	$\frac{\int_{1.315}^{1.34} f(\lambda)d\lambda}{\int_{1.26}^{1.285} f(\lambda)d\lambda}$	$\frac{\int_{1.18}^{1.23} f(\lambda)d\lambda}{2\int_{1.26}^{1.285} f(\lambda)d\lambda}$	$\frac{\int_{1.48}^{1.52} f(\lambda)d\lambda}{\int_{1.36}^{1.60} f(\lambda)d\lambda}$	$\frac{\int_{1.635}^{1.675} f(\lambda)d\lambda}{\int_{1.56}^{1.60} f(\lambda)d\lambda}$	$\frac{\int_{1.53}^{1.56} f(\lambda)d\lambda}{\int_{1.57}^{1.60} f(\lambda)d\lambda}$	$\frac{\int_{2.215}^{2.255} f(\lambda)d\lambda}{\int_{2.08}^{2.12} f(\lambda)d\lambda}$	$\frac{\int_{2.06}^{2.10} f(\lambda)d\lambda}{\int_{1.25}^{1.29} f(\lambda)d\lambda}$		
2MASS0415	0.030 (T8)	0.168 (T8)	0.31	0.173 (T8)	0.105 (T8)	0.625 ± 0.003	0.050 (>T7)	0.134	–	T8
ULAS0034	0.012 ± 0.006 (>T8)	0.144 ± 0.009 (>T8)	0.262 ± 0.006	0.133 ± 0.010 (>T8)	0.096 ± 0.006 (T8)	0.516 ± 0.008	0.091 ± 0.015 (>T7)	0.128 ± 0.003	>T8	T9
CFBDS0059	0.029 ± 0.005 (T8)	0.164 ± 0.008 (T8)	0.257 ± 0.004	0.119 ± 0.008 (>T8)	0.084 ± 0.002 (T8)	0.526 ± 0.005	0.128 ± 0.037 (>T7)	0.101 ± 0.002	>T8	T9
ULAS1017	0.054 ± 0.007 (T8)	0.156 ± 0.006 (T8)	0.347 ± 0.005	0.274 ± 0.016 (T6)	0.309 ± 0.011 (T6)	0.688 ± 0.017	0.174 ± 0.018 (T6)	0.119 ± 0.002	T8/T6	T8p
ULAS1238	0.043 ± 0.008 (T8)	0.218 ± 0.009 (T7)	0.284 ± 0.006	0.145 ± 0.013 (>T8)	0.085 ± 0.009 (T8)	0.601 ± 0.013	0.083 ± 0.012 (>T7)	–	T8	T8.5
ULAS1335	0.034 ± 0.004 (T8)	0.179 ± 0.004 (T8)	0.254 ± 0.003	0.114 ± 0.004 (>T8)	0.077 ± 0.003 (T8)	0.564 ± 0.002	0.094 ± 0.007 (>T7)	0.134 ± 0.001	>T8	T9

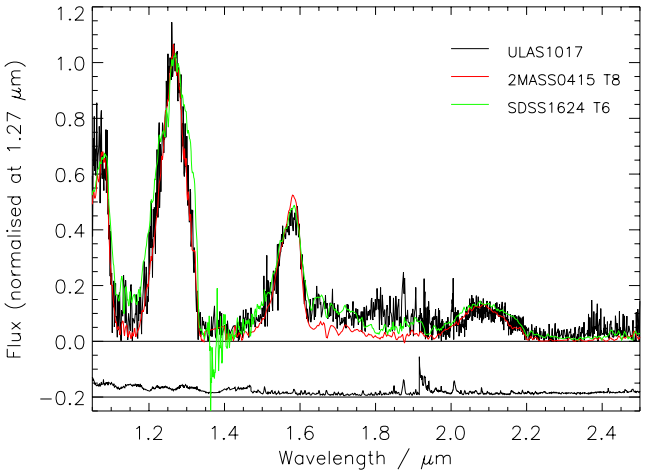

Figure 3. The IRCS + NIRI *JHK* spectrum of ULAS1017 (black line) overplotted with the spectra of the T8 standard 2MASS0415 and the T6 standard SDSS1624. The error spectrum, offset by −0.2 in the *y*-axis, is plotted as a black line.

et al. 2008), the late spectral type of this object would seem to preclude that interpretation. Pinfield et al. (2008) identified ULAS J1150+0949, a T6.5p with a similarly peculiar early *H*-band type (of T3 in this case), so such morphology may be a generic trait for some objects.

3.2 ULAS1238

Fig. 4 compares the *J*- and *H*-band flux peaks for ULAS1238 to those for 2MASS0415 and ULAS0034. Initial examination of these plots, and the spectral indices given in Table 5, suggest a spectral type of T8 for ULAS1238. Closer examination of the *H*-band peak reveals some similar narrow features in the spectra of ULAS0034 and ULAS1238. Additionally, the width of the *J*-band peak, and the values of the *H*-band spectral indices imply that ULAS1238 is in fact intermediate between ULAS0034 and 2MASS0415. If we adopt the type T9 for ULAS0034 (see Section 3.3), then ULAS1238 could reasonably be classified as T8.5. However, the inherently small changes in NIR spectral morphology in this regime make such distinctions non-critical in the absence of additional mid-IR spectral coverage.

3.3 ULAS1335

An initial inspection of the shapes of the *J*- and *H*-band flux peaks of ULAS1335 (see Fig. 5) indicates that it is of the same spectral type as ULAS0034 and CFBDS0059. In particular it should be noted that the strength of the absorption blueward of 1.565 μm that Delorme et al. (2008) attribute to NH_3 is similar for all three objects. Given the close similarity of these objects to the rest of the T dwarf sequence, it is appropriate that these objects form an extension of that sequence, and we assign to them the subtype T9. Fig. 6 shows the full *YJHK* comparison of ULAS1335, CFBDS0059, ULAS0034 and 2MASS0415. Although the shapes of the *H*-band peaks are similar for the three objects, their height relative to the *J*-band peak varies significantly. Specifically, ULAS1335 and CFBDS0059 both exhibit much stronger *H*-band peaks than either ULAS0034 or 2MASS0415.

In Fig. 7 we plot the *J*- and *H*-band spectral indices against the spectral types derived by template comparison for objects with types T6 to T9 (see below). It is apparent that the water and methane *J*-band indices previously used for the classifying T dwarfs are degenerate with type for the subtypes T8 and T9. Examination of Fig. 7 indicates that the same may be true for the CH_4–*H* index, although the H_2O–*H* index is still able to distinguish these objects. The new indices 'NH_3'–*H* and W_J both appear able to distinguish the T9 dwarfs from the earlier type objects; however, the 'NH_3'–*H* index is degenerate with type for the earlier objects.

In Fig. 8 we plot the 'NH_3'–*H* index against the W_J spectral index suggested by Warren et al. (2007). It is apparent that the latest objects are well separated from ≤T8 objects in this plot. However, the values of W_J and 'NH_3'–*H* do not show a consistent correlation for the latest objects. Fig. 9 shows the $H_2O - H$ index plotted with W_J. Again, the three latest objects are well separated from the other objects; however, in this case the values of the two indices show a clear trend (with the exception of the T8p dwarf), both decreasing together. The scatter in 'NH_3'–*H* values in Fig. 8, compared to the correlation shown in Fig. 9 thus suggests that although 'NH_3'–*H*

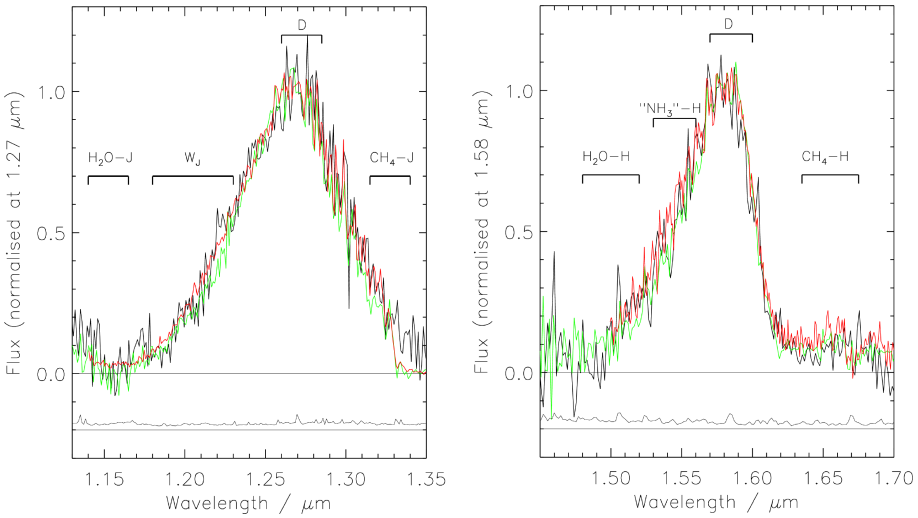

Figure 4. The *J*- and *H*-band flux peaks of ULAS1238 (black line), ULAS0034 (T9, see text; green line) and 2MASS0415 (T8; red line). The black line that is plotted offset by −0.2 in the *y*-axis is the error spectrum for ULAS1238. Also indicated are the spectral regions integrated to form the numerator of the spectral indices discussed in the text. The region that forms the denominator is indicated with the letter 'D'.

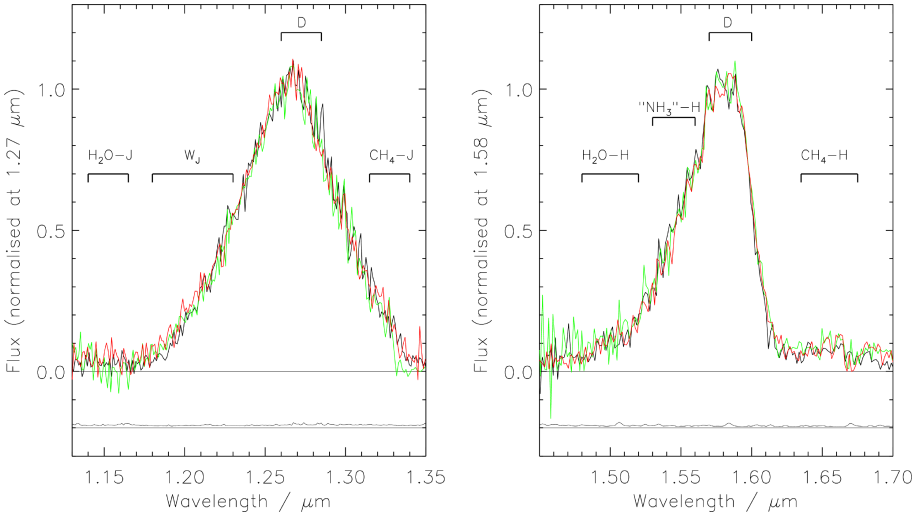

Figure 5. The *J*- and *H*-band flux peaks of ULAS1335 (black line), ULAS0034 (T9, see text; green line) and CFBDS0059 (T9, see text; red line). The black line that is plotted offset by −0.2 in the *y*-axis is the error spectrum for ULAS1335. Also indicated are the spectral regions integrated to form the numerator of the spectral indices discussed in the text. The region that forms the denominator is indicated with the letter 'D'.

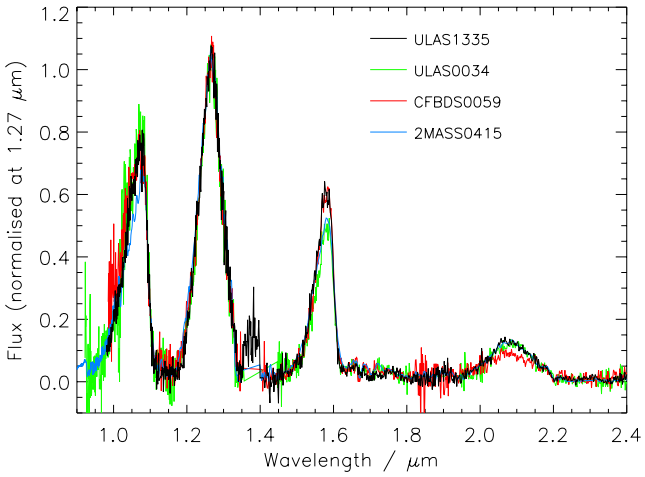

Figure 6. The full *YJHK* comparison of ULAS1335 to ULAS0034, CFBDS0059 and 2MASS0415.

is useful for identifying T8+ objects, it is not an effective typing index for very late objects in the range we are considering, and does not conveniently strap on to the previous T dwarf sequence.

We suggest that the appropriate spectral indices for the extension of the T spectral class to T9 are H_2O–*H* and W_J. To provide continuity with the earlier T indices we define the range of W_J and H_2O–*H* for types T7–T9, matching our values to the H_2O–*H* values of Burgasser et al. (2006) for types T7 and T8, and using the apparent correlation in Fig. 9 to arrive at appropriate W_J values. Our proposed set of spectral indices for the latter portion of the T spectral sequence are summarized in Table 6. In this scheme, ULAS1335, as well as ULAS0034 and CFBDS0059, are all T9 dwarfs, which are our adopted types. Since ULAS1335 is significantly brighter than both ULAS0034 and CFBDS0059, we also propose ULAS1335 as the template for the T9 subtype.

In Section 5.2 we estimate a $T_{\rm eff}$ for ULAS1335 which is marginally cooler than the Warren et al. (2007) estimate for ULAS0034. This temperature sequence is well represented by the locations of the objects in Fig. 9, but not by the sequence shown in Fig. 8. If the 'NH_3'–*H* index is indeed tracing a broad ammonia absorption band, this suggests two things. First, it appears to develop at odds with the water absorption in the *J* band (which the W_J feature traces) and the H_2O–*H* absorption feature. Secondly, if the relative temperatures of ULAS0034 and ULAS1335 are to be believed, it does not correlate well with temperature.

There is some theoretical justification for expecting NIR ammonia absorption to be only weakly dependent on $T_{\rm eff}$. Ammonia chemistry is governed by upmixing, and in practice the mixing ratio depends most strongly on the ammonia abundance at the quench level. Since this is at a nearly fixed temperature, ∼2000 K, the remaining variables that will affect it are pressure and composition. Thus, we expect the ammonia mixing ratio, and by extension the strength of ammonia absorption in the NIR, to be far more sensitive to gravity and metallicity than $T_{\rm eff}$. Given this behaviour, there is exciting potential for the 'NH_3'–*H* index as an additional diagnostic tool for very cool T dwarfs, and its development will be followed with interest as more objects in the very low-temperature regime are identified.

4 SEARCHING FOR COMMON PROPER MOTION COMPANIONS

It has been known for some time that the degree of multiplicity amongst very young stars is greater than that of the more evolved field star populations (Duquennoy & Mayor 1991; Leinert et al. 1993), and thus that the majority of binary systems form together in their nascent clouds. Binary components can therefore generally be assumed to share the same age and composition, and wide common proper motion companions to our new objects could thus provide valuable constraints if they are to be found. In order to address this possibility and more generally assess the kinematics of our objects, we calculated proper motions for our targets using the highest signal-to-noise ratio multi-epoch observations available. In each case this was the WFCAM and UFTI *J*-band images.

The IRAF routines geomap and geoxytran were used to transform between the available multi-epoch images, using an average of 12 reference stars. This allowed any motion of the T dwarfs to be accurately measured. Proper motion uncertainties were estimated

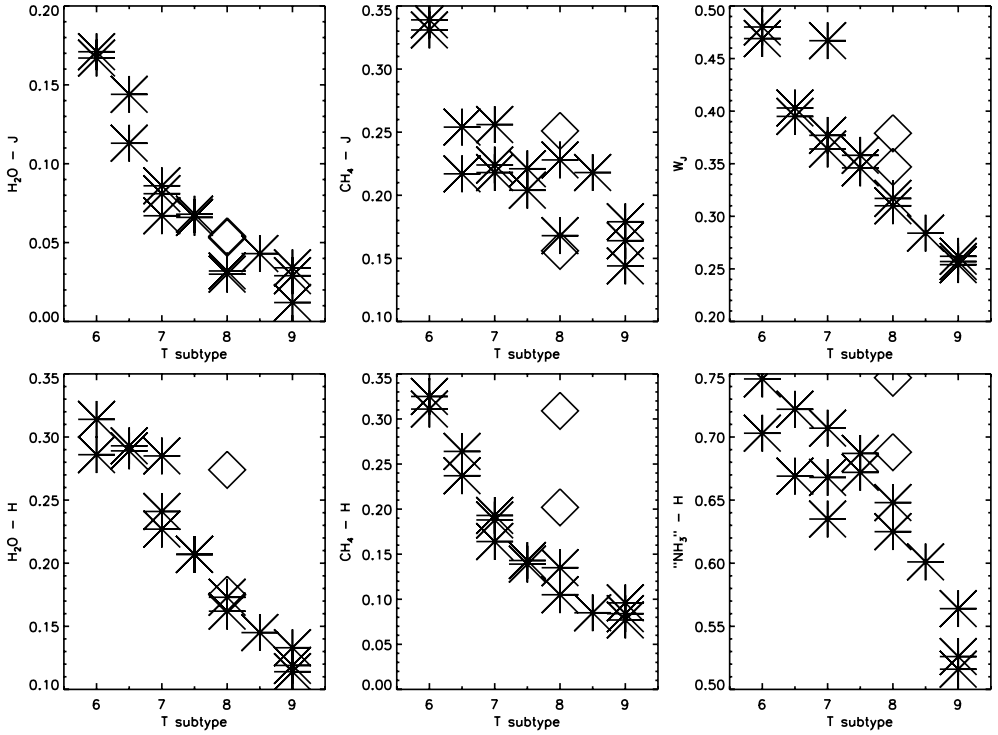

Figure 7. Spectral index versus T-subtype for T6–T9 dwarfs. Asterisks indicate 'normal' dwarfs, whilst the diamonds indicate two T8p dwarfs: ULAS1017 and 2MASS J07290002−3954043. Index values for these objects are drawn from Burgasser et al. (2006), Warren et al. (2007), Delorme et al. (2008) and Looper, Kirkpatrick & Burgasser (2007), or are calculated from the objects' spectra supplied by these authors. Uncertainties are smaller than the symbol sizes.

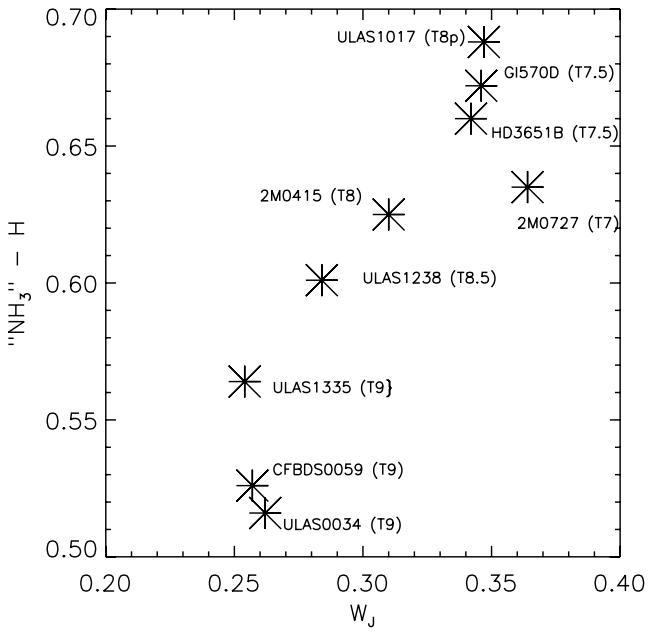

Figure 8. The 'NH_3'–*H* index versus W_J index. Uncertainties are not displayed as they are smaller than the symbol size.

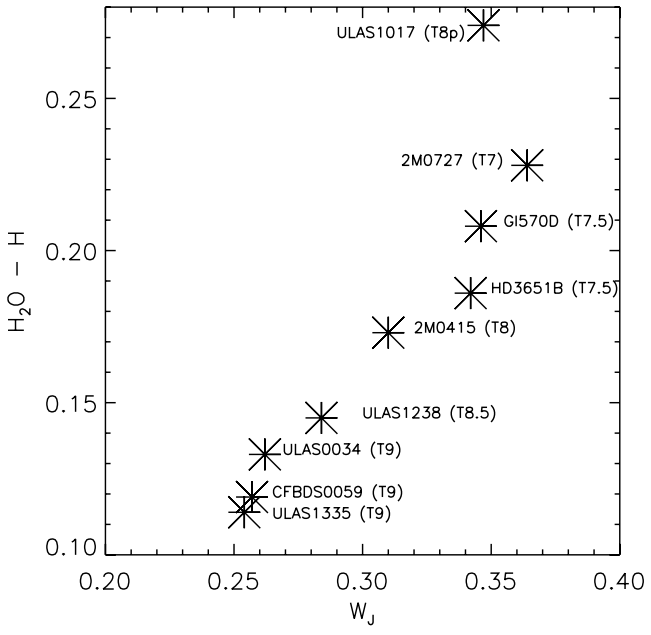

Figure 9. The H_2O–*H* index versus W_J index. Uncertainties are not displayed as they are smaller than the symbol size.

from centroiding accuracies combined with the residuals associated with our derived transformations. The calculated proper motions are given in Table 7. We also estimate $V_{\rm tan}$ based on our distance estimates derived in Section 7. These estimates lie within the range of $V_{\rm tan}$ observed by Vrba et al. (2004) for L and T dwarfs.

We independently searched the Supercosmos Sky Survey data base, and the Simbad data base (accessing the *Hipparcos* and Tycho catalogues amongst others), for common proper motion companions (within 1σ) of the three new T dwarfs, thus searching for wide binary companions over a wide range of mass. The search was made

Table 6. Our proposed spectral indices for the latter most portion of the T spectral sequence. Also given are the spectral type standards for each type.

NIR spectral type	H_2O-J	CH_4-J	W_J	H_2O-H	CH_4-H	CH_4-K	Standard
T7	0.07–0.13	0.21–0.28	0.35–0.40	0.20–0.26	0.15–0.25	<0.13	2MASS0727
T8	<0.07	<0.21	0.28–0.35	0.14–0.20	<0.15	–	2MASS0415
T9	–	–	<0.28	<0.14	–	–	ULAS1335

Table 7. Proper motion estimates for the three new T dwarfs. Uncertainties reflect the residuals in the transformations between the two images in each case. Also given are estimates for V_{tan} for ULAS1335 and ULAS1017 (see Section 7 for distances).

Object	First epoch coordinates		Epoch 1	Epoch 2	$\mu_{\alpha\cos\delta}$	μ_δ	V_{tan}
	α	δ			(mas yr^{-1})	(mas yr^{-1})	(km s^{-1})
ULAS1017	10 17 21.40	+01 18 17.9	2007-03-17	2008-01-17	110 ± 80	40 ± 80	4–58
ULAS1238	12 38 28.51	+09 53 51.3	2007-02-13	2008-01-25	418 ± 40	21 ± 40	–
ULAS1335	13 35 53.45	+11 30 05.2	2007-04-21	2008-01-16	160 ± 50	-290 ± 50	10–21

within a projected distance of 20 000 au from each target, calculated assuming the minimal distance within our derived constraints (see Section 7) to ensure a spatially complete search. In the case of ULAS1238 we used a lower distance estimate of 20 pc based on comparison with ULAS0034. SDSS and UKIDSS photometry were then retrieved for any common proper motion objects, and from these a spectral type range was estimated, and an approximate distance modulus inferred. Sources with distance moduli that were inconsistent with the inferred distances to our newly discovered dwarfs (see Section 7) could then be rejected as potential companions. Our search produced no potential companions for any of our targets.

5 ATMOSPHERIC PARAMETERS

In the following two sections we estimate the atmospheric parameters of ULAS1017 and ULAS1335 through model comparisons, and, in the case of ULAS1335, consideration of the NIR to mid-IR spectral energy distribution (SED). The model spectra we employ are a recent realization of the BT-Settl models, for which detailed descriptions of the input physics are given in Warren et al. (2007) and Allard et al. (in preparation). There are uncertainties in these models that limit their use significantly for simplistic comparisons, but by limiting our analysis to relative comparisons over key spectral ranges, and some extrapolation of theoretical trends, we are able to derive a set of 'best guess' properties based on the existing theoretical and observational data.

We do not perform a detailed analysis for ULAS1238 due to the absence of *K*-band photometry that precludes flux calibration for this part of the spectrum. Instead we speculate that its properties are likely intermediate between 2MASS0415 and ULAS0034 since its spectral type is also intermediate. However, we do not rule out the possibility of a considerably lower T_{eff} (see Section 6).

5.1 ULAS1017

To estimate the atmospheric parameters for ULAS1017 we repeat the $(W_J, K/J)$ analysis described by Warren et al. (2007) for ULAS0034, and applied to CFBDS0059 by Delorme et al. (2008). To this end we have calculated W_J and *K*/*J* indices for a grid of solar metallicity BT-Settl models with $4.20 < \log g < 5.50$ and $600 < T_{eff} < 900$ K. We have anchored the resulting $(W_J, K/J)$ grid such that $T_{eff} = 750K$ and $\log g = 5.0$ for the empirical $(W_J, K/J)$ coordinates of 2MASS0415, consistent with the detailed analysis of Saumon et al. (2007). Placing ULAS1017 on this grid implies a $T_{eff} = 800$ K and $\log g = 5.5$ (see Fig. 10).

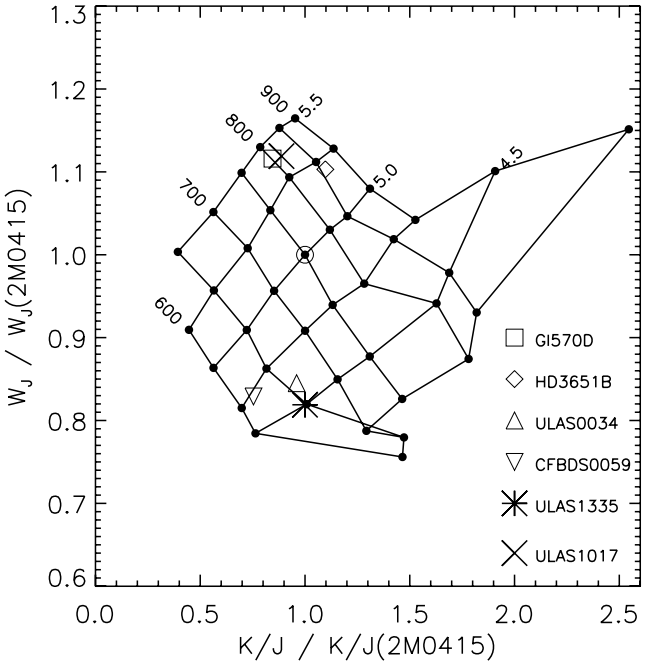

Figure 10. W_J versus *K*/*J* indices for a grid of solar metallicity BT-Settl model spectra. The grid has been normalized by matching the $T_{eff} = 750$ K, $\log g = 5.0$ model indices to the empirical index values for 2MASS0415, which lies at (1.0, 1.0).

In Fig. 11 we compare the spectrum of ULAS1017 to model spectra that bracket its location in the $(W_J, K/J)$ plane. It appears that the model spectra generally fit the spectrum of ULAS1017 well. We note, however, that it is the model for $T_{eff} = 800$ K and $\log g = 5.0$ that provides the best-fitting spectrum, in contrast to the $(W_J, K/J)$ analysis that suggests $\log g = 5.5$.

The location of ULAS1017 in Fig. 10 is very close to that of Gl 570D. It is worth noting that using detailed analysis with

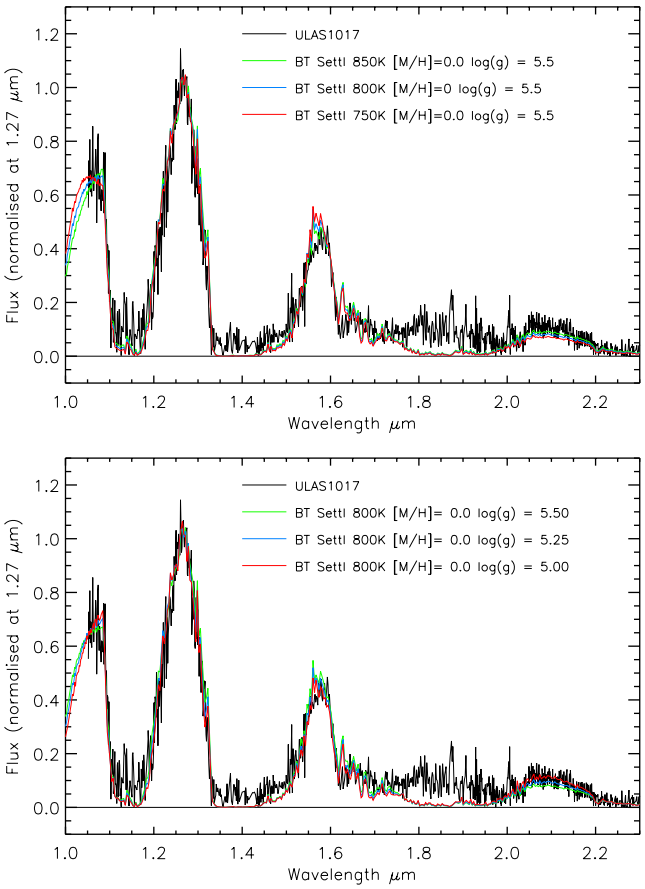

Figure 11. A comparison of model spectra for the parameters bracketing the location of ULAS1017 in the solar metallicity $(W_J, K/J)$ plane.

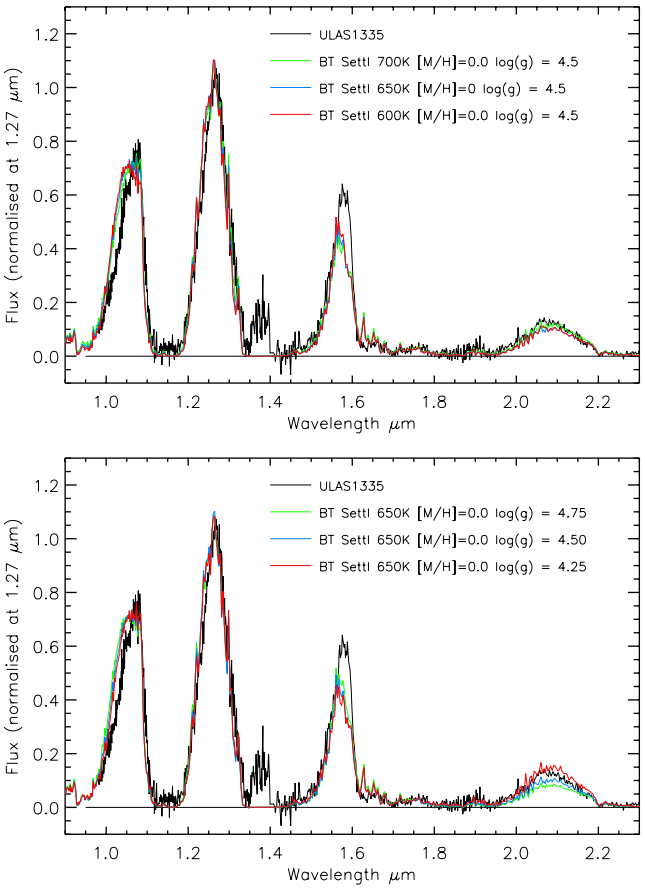

Figure 12. A comparison of model spectra for parameters bracketing the location of ULAS1335 in the solar metallicity $(W_J, K/J)$ plane.

consideration of non-equilibrium effects, Saumon et al. (2006) derive parameters for Gl 570D of $T_{\rm eff} = 800$–820 K and $\log g = 5.09$–5.23. This is very similar to our best value from spectral comparison for ULAS1017, but similarly at odds with the parameters from simple $(W_J, K/J)$ analysis.

Note also that this form of analysis can only provide approximate estimates of the atmospheric parameters, and it must be remembered that varying estimates of surface gravity will be degenerate with respect to varying metallicity. The lack of *Y*-band coverage in our spectrum of ULAS1017 prevents us from making any estimate of its metallicity relative to other objects based on the form of its *Y*-band peak. Furthermore, the form of the *H*-band flux peak, resembling that of a T6 dwarf adds an additional element of uncertainty to our 'best guess' properties for this object.

5.2 ULAS1335

We will begin by placing ULAS1335 on the $(W_J, K/J)$ grid (see Fig. 10), which implies $T_{\rm eff} \approx 650$K and $\log g \approx 4.5$. To assess the credence of these theoretical predictions, Fig. 12 shows the comparison of ULAS1335 with the BT-Settl synthetic spectra for the atmospheric parameters that bracket its location in the $(W_J, K/J)$ plane for solar metallicity. It is clear that these synthetic spectra are not a good fit to the data. The most obvious discrepancy is the height of the *H*-band flux peak. It is widely acknowledged that the shape of the *H*-band peak is poorly reproduced by model spectra, a fact that is attributed to incomplete methane line lists. However, in the cases of ULAS0034, CFBDS0059 and 2MASS0415, the observed height of the *H*-band flux peak is well represented by the model spectra for the atmospheric parameters estimated from their location in the $(W_J, K/J)$ plot (see Warren et al. 2007; Delorme et al. 2008, figs 6 and 7, respectively). It is thus clear that despite many similarities between ULAS1335 and the other two T9 dwarfs, its *H*-band peak is, by comparison, significantly brighter. Some of the properties of ULAS1335 are thus presumably somewhat different to the other two T9 dwarfs.

We can make a first assessment of possible differences in metallicity by considering the shape of the *Y*-band peak. All available theoretical models indicate that the shape of this flux peak will be sensitive to [M/H], although there is some ambiguity as to exactly how compositional changes will affect its shape. A comparison of the *Y*-band peaks of the three T9 dwarfs in Fig. 6 reveals them to have an extremely similar *Y*-band spectral morphology, and it thus seems unlikely that these objects have significantly different metallicity.

Fig. 12 shows what changes we might expect for varying $\log g$ and $T_{\rm eff}$. In the bottom plot it can be seen that although a higher gravity can increase the brightness of the *H*-band peak relative to the *J*- and *Y*-band peaks, it has the opposite effect on the *K*-band flux peak. These trends thus indicate that it is not possible to theoretically account for the relatively bright *H*-band peak of ULAS1335 compared to the other T9 dwarfs, simply by varying $\log g$ alone.

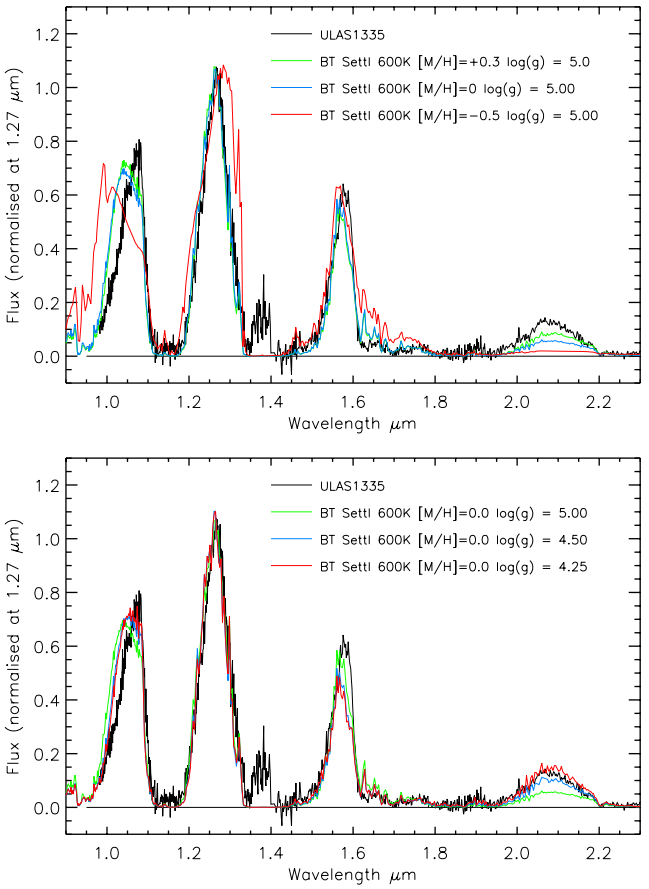

Figure 13. A comparison of model spectra with ULAS1335 for differing gravity and metallicity combinations at $T_{\rm eff} = 600$ K.

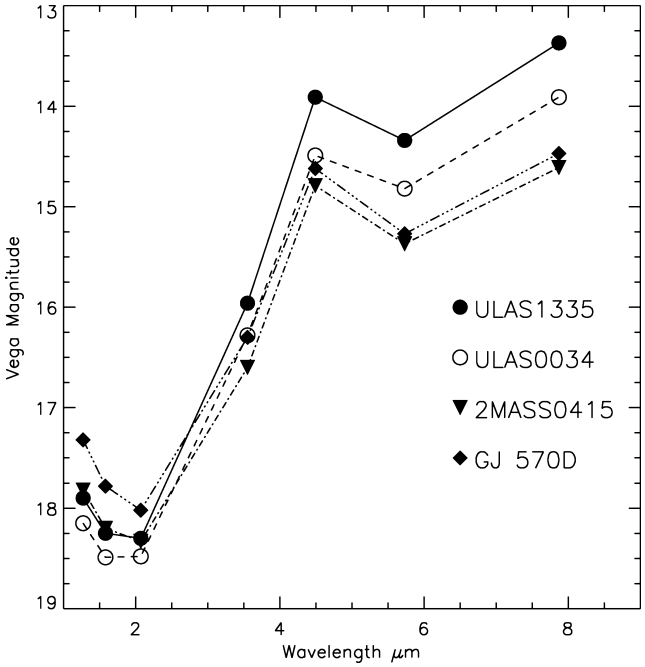

Figure 14. The 1–8 μm SEDs for ULAS1335, ULAS0034 (Warren et al. 2007), 2MASS0415 and Gl 570D. The photometry for the latter two objects, taken from Leggett et al. (2002) and Patten et al. (2006), has been offset by +2.5 mag to allow comparison with the T8+ dwarfs. Uncertainties are of comparable size to the symbols.

We can obtain a better match between theoretical and observed spectra if we adopt a lower $T_{\rm eff}$ for ULAS1335. The top plot in Fig. 12 demonstrates the trend in the BT-Settl model spectra, and shows that the relative brightness of the *H*-band peak increases compared to the *Y*- and *J*-band peaks as $T_{\rm eff}$ decreases below 700 K. However, note that although there is some change to the relative strength of the *K*-band peak, it is not as drastic as when one varies $\log g$. The overall NIR morphology of ULAS1335 is thus best explained (through current theory) if this object has a somewhat lower $T_{\rm eff}$ than ULAS0034.

In Fig. 13 we compare the spectra of ULAS1335 to a range of model spectra with different metallicities and gravities for our lowest available temperature models, $T_{\rm eff} = 600$ K. In the top plot, the combination $\log g = 5.0, T_{\rm eff} = 600$ K model spectra all estimate the height of the *H*-band peak well. The subsolar metallicity model is a poor match everywhere else however. The high-metallicity model gives a reasonable approximation to the observed spectrum, but as expected it underestimates the *K*-band flux somewhat, and has a significantly wider and blueward shifted *Y*-band peak.

In the bottom plot, the $\log g = 4.25$–4.50 model spectra provide a reasonable fit to the whole NIR spectra. However, whilst reproducing the *Y*-, *J*- and *K*-band peaks, these spectra still somewhat underestimate the brightness of the *H*-band peak. Although the low $T_{\rm eff}$ of this model has gone some way to addressing the relative brightness of this peak, the model trends suggest that we should obtain a better fit by going to even lower $T_{\rm eff}$.

Investigation of the NIR to mid-IR SED for ULAS1335 reveals that is extremely red. Fig. 14 shows the 1–8 μm SEDs for ULAS1335, ULAS0034, 2MASS0415 and Gl 570D. Whilst the form of the SEDs are similar, ULAS1335 is significantly redder than ULAS0034 over the 2–4.49 μm range. ULAS1335 has $H - [4.49] = 4.34 \pm 0.04$, the reddest value yet observed for a T dwarf. Warren et al. (2007) identified a correlation between the $H - [4.49]$ colour and $T_{\rm eff}$ for T dwarfs with well-determined $T_{\rm eff}$ (Golimowski et al. 2004). In fact the correlation for T dwarfs with $T_{\rm eff} = 800$–1250 K is particularly tight, with an rms about the best-fitting linear relation of ± 28 K. In Fig. 15 we show this linear fit, and indicate the $H - [4.49]$ colours of 2MASS0415, ULAS0034 and ULAS1335. Theoretical tracks are also overplotted for a recent realization of the Marley et al. (2002) model atmospheres for the range 500–800 K (Marley & Saumon, private communication). Tracks are shown for $4.48 \leq \log g \leq 5.48$ and $-0.3 \leq$ [M/H] $\leq +0.3$, bracketing the expected properties of ULAS1335. We have anchored the models for $\log g = 5.0$ and solar metallicity to the colours of the coolest T dwarfs with well-determined temperatures. It can be seen that the theoretical models are reasonably supportive of an extrapolation of the relation between $H - [4.49]$ and $T_{\rm eff}$ for such $\log g$ and [M/H] ranges, and this extrapolation suggests that ULAS1335 has $T_{\rm eff} \sim$550–600 K.

In the case of ULAS0034, the temperature inferred by $(W_J, K/J)$ analysis was reasonably consistent with that inferred from an extrapolation of the $T_{\rm eff}$–$H - [4.49]$ relation. However, in the case of ULAS1335 we have seen that the two estimates differ by ∼100 K. The poor agreement between the model spectra for 650 K and the observed spectrum of ULAS1335 cast doubt on the temperature derived from the $(W_J, K/J)$ method. It is likely that this disagreement is principally due to the fact that T9 dwarfs are in the temperature range near the limit of where the NIR model spectra are valid.

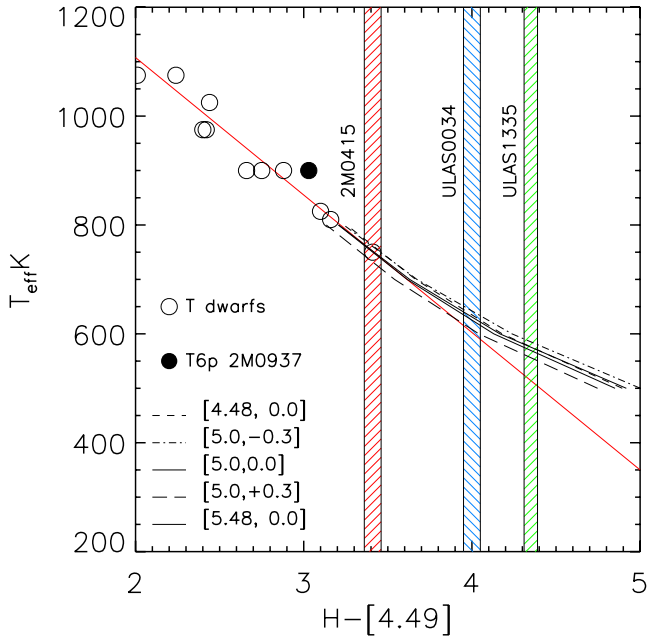

Figure 15. The $T_{\rm eff}$–$H-[4.49]$ relation for T dwarfs as defined by Warren et al. (2007). The shaded regions indicate the colours ($\pm1\sigma$) for the coolest T dwarfs with IRAC magnitudes. The straight red line indicates the empirical fit the colours of warmer T dwarfs. Also plotted, as black lines are theoretical tracks from Marley et al. (2002) and Marley & Saumon (private communication). Values for log g and metallicity are indicated in brackets.

Since no model spectra cooler than 600 K are plotted, a degeneracy in $(W_J, K/J)$ for these temperatures cannot be ruled out. Indeed, Fig. 10 indicates that there is a predicted distortion in the grid (which will result in some degeneracy) for the lowest gravity and temperature combinations currently considered.

The strong, relatively tight $T_{\rm eff}$ correlation offered by observed T dwarf $H-[4.49]$ colours combined with the theoretical expectations for a reasonably steady shift of flux from the NIR into the mid-IR with decreasing $T_{\rm eff}$, lends weight to this colour as a better temperature indicator for such very late objects, and we adopt the temperature implied by this colour rather than that implied by the $(W_J, K/J)$ method. We also suggest that the $(W_J, K/J)$ method be used with caution in the $T_{\rm eff}$ regime near the limit of current atmospheric models.

To summarize, our comparison to model NIR spectra suggested that ULAS1335 has $T_{\rm eff} < 600$ K. This is clearly supported by the NIR-to-mid-IR SED, which suggests $T_{\rm eff} \sim 550$–600 K from a theoretically informed extrapolation. Our 'best guess' for the temperature of ULAS1335 is thus $T_{\rm eff} \sim 550$–600 K.

This temperature is stated along with an important caveat. We note that preliminary investigations of recent realizations of the Marley et al. (2002) model spectra (Marley & Saumon, private communication) do not show the same trends with varying parameters in the NIR as the BT-Settl models. Although we defer a detailed comparison of these model spectra with the BT-Settl models to a future work, we highlight those differences of particular relevance here. Most notable is the absence of a trend of increasing height of the H-band peak with decreasing $T_{\rm eff}$. In addition the height of the H-band peak appears more strongly dependent on metallicity than in the BT-Settl models, increasing with decreasing metallicity.

Finally, considering the absence of mid-IR photometry for CFBDS0059, and the reliance on the $(W_J, K/J)$ method for its temperature estimate, we also note that no strong conclusion regarding its temperature relative to ULAS1335 and ULAS0034 should be drawn. We cannot rule out the possibility that CFBDS0059 is cooler still.

6 COMPARISON WITH THE JOVIAN SPECTRUM

We have also examined our T dwarf spectra in more detail, to try and identify new features that might be useful in this new $T_{\rm eff}$ regime. We follow Leggett et al. (2007a) and use the spectrum of Jupiter along with transmission spectra of ammonia and methane as a basis for comparison, which we plot in Fig. 16 alongside ULAS0034, CFBDS0059, ULAS1238 and ULAS1335. Although the metallicity of the Jovian atmosphere is much higher, and the gravity much lower, than that expected for our T dwarfs, this comparison with a much cooler atmosphere is still interesting.

We draw attention to the narrow feature near 1.23 μm (leftmost vertical green line in Fig. 16) which appears to be shared by Jupiter, ULAS1238 and ULAS1335. This should not be confused with the K I doublet at ∼1.24–1.25 μm. We attribute this feature to methane, based on comparison with the laboratory transmission spectrum of Cruikshank & Binder (1969). We also highlight the narrow feature at ∼1.272 μm (rightmost vertical green line), which also appears to be common between ULAS1238, ULAS1335 and Jupiter. This may be due to ammonia, based on comparison to the transmission spectrum of Irwin et al. (1999). We note, however, that the sharp feature blueward of this (indicated by a vertical red line); also likely due to ammonia is apparently absent from the spectra of the T dwarfs.

7 PHYSICAL PARAMETERS

Since metallicity is thought to only weakly impact the derivation of fundamental parameters from $T_{\rm eff}$ and log g (e.g. Saumon et al. 2007), we use the solar metallicity relations summarized by Burrows et al. (2001) to estimate the mass, age and radius for ULAS1017 and ULAS1335 from our $T_{\rm eff}$ and log g estimates.

For ULAS1017, the extreme cases from the model comparison, $T_{\rm eff} = 750$–850 K and $\log g = 5.0$–5.5 correspond to an age of 1.6–15 Gyr and a mass of 33–70M_J. By estimating its radius from the same set of relations, and normalizing the corresponding atmospheric models to the J-band flux peak, we can estimate the distance to ULAS1017 to be in the range 31–54 pc.

For ULAS1335, we use our best estimate of $T_{\rm eff} = 550$–600 K and, since we suspect low gravity for this object, we adopt a conservative range of $\log g = 4.5$–5.0 for its surface gravity. These atmospheric parameters only weakly constrain the age to a range of 0.6–5.3 Gyr and the mass to 15–31M_J.

In the absence of model spectra for $T_{\rm eff} < 600$ K, we have estimated the bolometric flux for ULAS1335 using a pseudo-synthetic spectrum. This was constructed by bracketing our flux-calibrated *YJHK* spectrum with the model spectrum for $T_{\rm eff} = 600$ K and $\log g = 4.5$, scaling the synthetic parts with our z-band photometry in the optical and our IRAC [4.49] photometry in the mid-IR. We then integrated this pseudo-synthetic spectrum over all wavelengths to estimate the bolometric flux from ULAS1335. The uncertainty in this estimate is dominated by uncertainty in the photometry used to calibrate the spectrum. These uncertainties range from 10 per cent for the optical photometry to <5 per cent for our NIR photometry. These regions contribute ∼0.5 and 25 per cent to the bolometric flux estimate, respectively. The mid-IR, which contributes ∼75 per cent

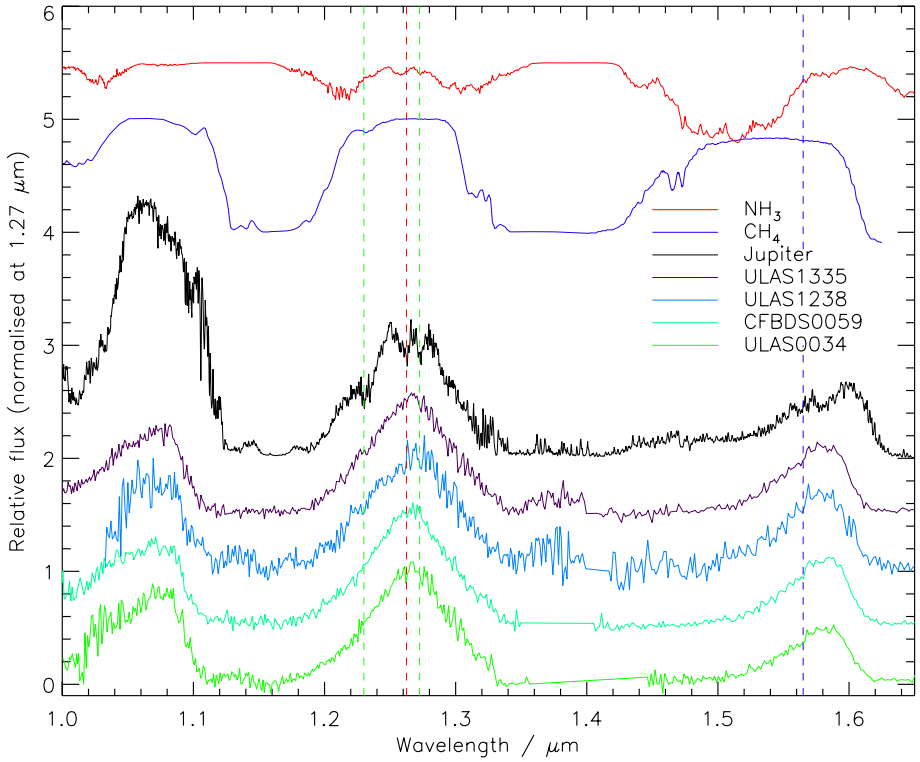

Figure 16. Spectra for ULAS0034, CFBDS0059, ULAS1238 and ULAS1335 compared with the NIR spectrum of Jupiter (Rayner, Cushing & Vacca, in preparation) and laboratory transmission spectra of methane (Cruikshank & Binder 1969) and ammonia (Irwin et al. 1999). The vertical green dashed lines highlight narrow features that appear to be common to ULAS1238, ULAS1335 and Jupiter. The vertical red dashed line highlights an interesting feature in the Jovian spectrum that is absent from the T dwarf spectra (see text). The vertical blue dotted line indicates the location of the red edge of the broad absorption attributed to ammonia by Delorme et al. (2008).

Table 8. A summary of our estimates for the properties of ULAS1017 and ULAS1335. Estimates for ULAS1238 have been generally neglected in the absence of full flux calibrated spectral coverage. Distances assume that the dwarfs are single objects.

Object	Spectral type	$T_{\rm eff}$ (K)	$\log g$ [log(cm s^{-2})]	Mass (M_J)	Age (Gyr)	Distance (pc)
ULAS1017	T8p	750–850	5.0–5.5	33–70	1.6–15	31–54
ULAS1335	T9	550–600	<5.0	15–31	0.6–5.3	8–12

of the bolometric flux, has an uncertainty of 4 per cent in its [4.49] mag, which we use to scale the synthesized spectrum. Allowing for additional uncertainty in the model spectrum match to the true mid-IR spectrum, we estimate a total uncertainty in our bolometric flux to be ∼15 per cent, and the bolometric flux to be $F_{\rm bol} = 3.35 \pm 0.5 \times 10^{-16}$ W m^{-2}.

The uncertainty in our distance estimate for ULAS1335 is dominated by the uncertainty in $T_{\rm eff}$ (and thus luminosity). For $T_{\rm eff} = 550$–600 K and $\log g = 4.5$–5.0 we estimate a luminosity of $-6.18 \leq \log(L_*/L_\odot) \leq -5.86$ (by inferring radii using the relations in Burrows et al. 2001) and thus a distance of 8–12 pc. Table 8 summarizes the inferred properties for the T dwarfs identified in this paper.

8 SUMMARY

We have identified three very late-type T dwarfs in the UKIDSS LAS DR3: ULAS1017, ULAS1238 and ULAS1335, for which we have adopted the spectral types T8p, T8.5 and T9, respectively. ULAS1017 has a peculiar spectrum, with a *J*-band typical of a T8 dwarf, but *H*- and *K*-band peaks of a T6. In assigning spectral types to our targets, we have defined the extension of the T-dwarf sequence to the type T9, using the H_2O–*H* and W_J indices, and ULAS1335 as the spectral standard.

To estimate atmospheric parameters for ULAS1017 and ULAS1335, we have performed a detailed comparison with BT-Settl model spectra. For ULAS1017, we have estimated that its temperature lies in the range $750 \leq T_{\rm eff} \leq 850$, with $\log g = 5.0$–5.5 (assuming solar metallicity).

Our model comparison for ULAS1335 has suggested a $T_{\rm eff}$ that is cooler than the coolest available BT-Settl models ($T_{\rm eff} < 600$ K), and it may have low surface gravity possibly combined with high metallicity. As a result we have based our 'best guess' of the atmospheric parameters on an examination of the NIR to mid-IR SED. We have found ULAS1335 to be the reddest T dwarf yet identified, with $H - [4.49] = 4.34 \pm 0.04$. By extrapolating the empirical $T_{\rm eff}$–$H - [4.49]$ relation to lower $T_{\rm eff}$, and guided by model trends, we have estimated that ULAS1335 has $T_{\rm eff} \sim 550$–600 K. This

estimate suggests that ULAS1335 is the coolest brown dwarf yet discovered, although we await the determination of its distance by parallax with interest.

ACKNOWLEDGMENTS

We wish to thank our anonymous referee for helpful suggestions that have improved the quality of this paper. We also thank P. Delorme for supplying us with an electronic version of the spectrum for CFBDS0059 for use in this paper. We are extremely grateful to D. Saumon and M. Marley for providing us with model $H - [4.49]$ colours for their latest set of ultracool dwarf atmospheres. The UKIDSS project is defined in Lawrence et al. (2007). UKIDSS uses the UKIRT Wide Field Camera (WFCAM; Casali et al. 2007) and a photometric system described in Hewett et al. (2006). The pipeline processing and science archive are described in Irwin et al. (2008) and Hambly et al. (2008). We have used data from the third data release, which is described in detail in Warren et al. (in preparation). This paper is based on observations made with the European Southern Observatory telescopes obtained from the ESO/ST-ECF Science Archive Facility. Results reported here are based on observations obtained at the Gemini Observatory under programme numbers GN-2007B-Q-26 and GN-2008A-Q-15. Gemini Observatory is operated by the Association of Universities for Research in Astronomy, Inc. (AURA), under a cooperative agreement with the NSF on behalf of the Gemini partnership: the National Science Foundation (United States), the Science and Technology Facilities Council (United Kingdom), the National Research Council (Canada), CONICYT (Chile), the Australian Research Council (Australia), Ministrio da Cincia e Tecnologia (Brazil) and SECYT (Argentina). SKL is supported by the Gemini Observatory, which is operated by AURA, on behalf of the international Gemini partnership of Argentina, Australia, Brazil, Canada, Chile, the United Kingdom and the United States of America. DBN is supported by Ministerio de Ciencia e Innovación (Spain). This research has made use of the SIMBAD data base, operated at CDS, Strasbourg, France. Research has benefited from the M, L and T dwarf compendium housed at DwarfArchives.org and maintained by Chris Gelino, Davy Kirkpatrick and Adam Burgasser. This research has benefited from the SpeX Prism Spectral Libraries, maintained by Adam Burgasser at http://www.browndwarfs.org/spexprism.

REFERENCES

Burgasser A. J. et al., 2002, ApJ, 564, 421
Burgasser A. J., Geballe T. R., Leggett S. K., Kirkpatrick J. D., Golimowski D. A., 2006, ApJ, 637, 1067
Burgasser A. J., Liu M. C., Ireland M. J., Cruz K. L., Dupuy T. J., 2008, ApJ, 681, 579
Burrows A., Hubbard W. B., Lunine J. I., Liebert J., 2001, Rev. Mod. Phys., 73, 719
Burrows A., Burgasser A. J., Kirkpatrick J. D., Liebert J., Milsom J. A., Sudarsky D., Hubeny I., 2002, ApJ, 573, 394
Casali M. et al., 2007, A&A, 467, 777
Cruikshank D. P., Binder A. B., 1969, Commun. Lunar Planet. Lab., 6, 275
Delorme P. et al., 2008, A&A, 482, 961
Duquennoy A., Mayor M., 1991, A&A, 248, 485
Dye S. et al., 2006, MNRAS, 372, 1227
Fazio G. G. et al., 2004, ApJS, 154, 10
Golimowski D. A. et al., 2004, AJ, 127, 3516
Hambly N. C. et al., 2008, MNRAS, 384, 637
Hewett P. C., Warren S. J., Leggett S. K., Hodgkin S. T., 2006, MNRAS, 367, 454
Hodapp K. W. et al., 2003, PASP, 115, 1388
Irwin P. G. J., Calcutt S. B., Sihra K., Taylor F. W., Weir A. L., Ballard J., Johnston W. B., 1999, J. Quant. Spectrosc. Radiat. Transfer, 62, 193
Kendall T. R. et al., 2007, A&A, 466, 1059
Kirkpatrick J. D. et al., 1999, ApJ, 519, 802
Kobayashi N. et al., 2000, in Alan F. Moorwood, Iye M., Moorwood A. F., eds, Proc. SPIE Vol. 4008, Optical and IR Telescope Instrumentation and Detectors. SPIE, Bellingham WA, p. 1056
Lawrence A. et al., 2007, MNRAS, 379, 1599
Leggett S. K. et al., 2002, ApJ, 564, 452
Leggett S. K. et al., 2006, MNRAS, 373, 781
Leggett S. K., Marley M. S., Freedman R., Saumon D., Liu M. C., Geballe T. R., Golimowski D. A., Stephens D. C., 2007a, ApJ, 667, 537
Leggett S. K., Saumon D., Marley M. S., Geballe T. R., Golimowski D. A., Stephens D., Fan X., 2007b, ApJ, 655, 1079
Leinert C., Zinnecker H., Weitzel N., Christou J., Ridgway S. T., Jameson R., Haas M., Lenzen R., 1993, A&A, 278, 129
Lodieu N. et al., 2007, MNRAS, 379, 1423
Looper D. L., Kirkpatrick J. D., Burgasser A. J., 2007, AJ, 134, 1162
Looper D. L., Gelino C. R., Burgasser A. J., Kirkpatrick J. D., 2008, ApJ, 685, 1183
Manchado A. et al., 1998, in Albert M. Fowler, Fowler A. M., eds, Proc. SPIE Vol. 3354, Infrared Astronomical Instrumentation. SPIE, Bellingham WA, p. 448
Marley M. S., Seager S., Saumon D., Lodders K., Ackerman A. S., Freedman R. S., Fan X., 2002, ApJ, 568, 335
Moorwood A. et al., 1998, The Messenger, 94, 7
Patten B. M. et al., 2006, ApJ, 651, 502
Pinfield D. J. et al. 2008, MNRAS, 390, 304
Roche P. F. et al., 2003, in Iye M., Moorwood A. F. M., eds, Proc. SPIE Vol. 4841, Instrument Design and Performance for Optical/Infrared Ground-based Telescopes. SPIE, Bellingham WA, p. 901
Saumon D., Marley M. S., Cushing M. C., Leggett S. K., Roellig T. L., Lodders K., Freedman R. S., 2006, ApJ, 647, 552
Saumon D. et al., 2007, ApJ, 656, 1136
Vrba F. J. et al., 2004, AJ, 127, 2948
Warren S. J. et al., 2007, MNRAS, 381, 1400

This paper has been typeset from a TEX/LATEX file prepared by the author.